Dear Author:

Thank you for publishing with AGU. Your proofs are attached. Following the annotation guidelines and returning the proofs quickly will allow prompt online posting of the final version of your paper.

We have added several new features to the journal Web sites and additional services that we want to bring to your attention. The online version of your paper is enhanced in several ways, and will now include "Altmetrics," which continually tracks and links to mentions in news outlets, twitter, blogs, and other social media. A link to scholarly citations is also provided. Papers are also available in a regular PDF and as a Readcube version, which includes the Altmetrics and dynamic links to references and figures.

Please follow our social media sites! Several of our journals have social media sites; these and other AGU sites are indexed here.

If you have not already, we encourage you to create an ORCID (Open Researcher and Contributor ID) so that your work can be uniquely tracked. Your ORCID can be created and linked through your GEMS account.

Finally, your feedback is important to us. If you have questions or comments regarding your AGU Publications experience, including information on production and proofs, please contact us at publications@agu.org. We will also be contacting you soon after your article is published with an author survey. Please take a few minutes to respond to this online survey; your input is important in improving the overall editorial and production process.

Thank you again for supporting AGU.

Sincerely,

Brooks Hanson
Director, Publications AGU
bhanson@agu.org

2000 Florida Avenue, NW, Washington, DC 20009-1277
Tel: 202.462.6900
Fax: +1 202.328.0566
www.agu.org

PUBLICATION FEE CONSENT FORM

Dear Author:

As documented on the Steps to Publications webpage, content accepted for publication in an AGU journal may be subject to publication fees. The current fee schedule for AGU journalsis available from the Author Resources webpage.

This consent form has been generated for you in accordance with this policy on the basis of the final word, table, and figure counts of your article. The word count is for the abstract, body text, and captions only. Please review the calculated publication fee below, complete any relevant fields necessary for us to process your final invoice, and return a signed copy of this form to the production editor with your proof corrections. A final invoice will be mailed to the named billing contact within a few weeks of your articles appearance online in edited format.

Please note: OnlineOpen, the open access option for AGU journals, must be purchased through the OnlineOpen order form (https://authorservices.wiley.com/bauthor/onlineopen_order.asp).If you elected OnlineOpen at any earlier phase of submission and have not already submitted your order online, please do so now. Authors who select OnlineOpen will not be charged any base publication fee, but excess length fees will still apply.

ARTICLE DETAILS

Journal: Geochemistry, Geophysics, Geosystems

Article: Motoki, M. H., and M. D.Ballmer (2015), Intraplate volcanism due to convective instability of stagnant slabs in the mantle transition zone, *Geochem. Geophys. Geosyst.*, *16*, doi:10.1002/2014GC005608.

Words: 6,643

Figures: 7

Tables: 2

OnlineOpen: No

Publishing Units: 22

Excess Publishing Units: 0

Publication Fee: $1000

BILLING DETAILS

Name: ____________________

Address: ____________________

____

____

Signature: ____________________

Phone: ____________________

Email: ____________________

Date ____________________

AGU PUBLICATIONS

Geochemistry, Geophysics, Geosystems

RESEARCH ARTICLE

10.1002/2014GC005608

Intraplate volcanism due to convective instability of stagnant slabs in the mantle transition zone

Matthew H. Motoki[1] and Maxim D. Ballmer[1,2] AQ8

[1]Department of Geology and Geophysics, School of Ocean and Earth Sciences and Technology, University of Hawaii at Manoa, Honolulu, Hawaii, USA, [2]Earth-Life Science Institute, Tokyo Institute of Technology, Meguro, Tokyo, Japan

Key Points:

- Slabs that stagnate at the base of the upper mantle can go convectively unstable
- Related upwellings may sustain decompression melting and intraplate volcanism
- Convective instability can disrupt the slab's compositional stratification

Correspondence to:
M. D. Ballmer,
ballmer@elsi.jp

Citation:
Motoki, M. H., and M. D. Ballmer (2015), Intraplate volcanism due to convective instability of stagnant slabs in the mantle transition zone, *Geochem. Geophys. Geosyst.*, *16*, doi:10.1002/2014GC005608.

Received 10 OCT 2014
Accepted 23 JAN 2015
Accepted article online 30 JAN 2015

Abstract The study of volcanism can further our understanding of Earth's mantle processes and composition. Continental intraplate volcanism commonly occurs above subducted slabs that stagnate in the Mantle Transition Zone (MTZ), such as in Europe, eastern China, and western North America. Here, we use two-dimensional numerical models to explore the evolution of stagnant slabs in the MTZ and their potential to sustain mantle upwellings that can support volcanism. We find that weak slabs may go convectively unstable within tens of million years. Upwellings rise out of the relatively warm underbelly of the slab, are entrained by ambient-mantle flow and reach the base of the lithosphere. The first and most vigorous upwellings rise adjacent to lateral heterogeneity within the slab. Ultimately, convective instability also acts to separate the compositional components of the slab, harzburgite, and eclogite, from each other with harzburgite rising into the upper mantle and eclogite sinking into the lower mantle. Such a physical filtering process may sustain a long-term compositional gradient across the MTZ.

1. Introduction

Volcanism far away from tectonic-plate boundaries can inform about mantle processes and composition. Whereas the occurrence of age-progressive volcano chains with activity at localized hotspots is well explained by mantle plumes that rise from the lowermost mantle [*Wilson*, 1963; *Morgan*, 1972; *Griffiths*, 1986; *Torsvik et al.*, 2006; *Ballmer et al.*, 2013b], the origin of nonhotspot intraplate volcanism remains poorly understood and controversial. Mechanisms invoked for nonhotspot volcanism include (1) sublithospheric convective instability, (2) buoyant decompression melting, (3) shear-driven upwelling, and (4) lithospheric cracking. For example, sublithospheric instabilities (1) such as small-scale convection [*Richter and Parsons*, 1975; *Bonatti and Harrison*, 1976; *Buck and Parmentier*, 1986; *Rabinowicz et al.*, 1993; *Ballmer et al.*, 2007] (or delamination [*Houseman et al.*, 1981; *Gogus and Pysklywec*, 2008]) induce passive upwelling and decompression melting in response to downwelling of the negatively buoyant, cool sublithospheric mantle (or lithosphere itself). Analogously, buoyant decompression melting (2) can cause active upwelling due to instability of a positively buoyant layer of preexisting partial melt [*Tackley and Stevenson*, 1993; *Raddick et al.*, 2002; *Hernlund et al.*, 2008]. In contrast, the energy sources for shear-driven upwelling (3) and lithospheric cracking (4) are independent of density inversions in the mantle: the former (3) requires horizontal shear-driven or pressure-driven asthenospheric flow to be vertically redirected along steps of lithospheric thickness and/or mantle viscosity anomalies [*Conrad et al.*, 2010; *Bianco et al.*, 2011; *Ballmer et al.*, 2013a]. The latter (4) invokes tectonic stresses to crack the plate [*Sandwell et al.*, 1995; *Hieronymus and Bercovici*, 1999, 2000] and to allow extraction of preexisting melts that pond at the base of the lithosphere [e.g., *Sakamaki et al.*, 2013]. In the absence of strong thermal anomalies (as would be related e.g., to a mantle plume), all these mechanisms call for mantle materials to be at ((2), (4)), or at least close to ((1), (3)) the solidus.

Analysis of the spatiotemporal patterns of nonhotspot intraplate volcanism can serve to distinguish its dynamical origin. For example, ocean island chains with coeval volcanic activity over distances $\geq$1500 km—such as documented along the subparallel trends of the Marshalls and the Cook-Austral Islands—have been explained by small-scale convection with active decompression melting along one (or multiple parallel) "hot line(s)" [*Bonatti and Harrison*, 1976; *Ballmer et al.*, 2009, 2010]. Small volcanic provinces with short-lived activity <10 Myrs such as the Marquesas Islands have instead been associated with buoyant decompression melting [*Raddick et al.*, 2002]. Finally, volcanic ridges that display some form of age progression, but lack the specific features (in terms of direction and speed of progression) that are predicted for hotspot chains, have been related to lithospheric cracking [*Sandwell et al*., 1995; *Hieronymus and Bercovici*, 2000; *Cormier et al*., 2011], or shear-driven upwelling [*Bianco et al*., 2011; *Ballmer et al*., 2013a].

On the global scale, intraplate nonhotspot volcanism tends to be regionally clustered. For example, basaltic (i.e., presumably mantle-derived) intraplate volcanism on continents is focused in western North America (www.navdat.org), eastern Australia [*Wellman and McDougall*, 1974; *Johnson*, 1989], eastern China [*Zhou and Armstrong*, 1982; *Lei and Zhao*, 2005], and central Europe [*Wilson and Downes*, 2006; *Lustrino and Wilson*, 2007]. All these regions are underlain by subducted slabs (i.e., the Farallon, Pacific, and Alpine slabs, respectively) that stagnate in the MTZ [*Piromallo and Faccenna*, 2004; *Sigloch et al*., 2008; *Fukao and Obayashi*, 2013]. In many cases, volcanic activity has been specifically related to the toes of the slabs at the base of the upper mantle [*Piromallo and Faccenna*, 2004; *Wilson and Downes*, 2006; *Faccenna et al*., 2010; *Lei*, 2012] or slab windows [*Liu and Stegman*, 2012].

Volcanism directly above stagnant slabs or near their toes has commonly been related to upward mantle return flow in response to slab downwelling [*Faccenna et al*., 2010; *Kameyama and Nishioka*, 2012; *Tang et al*., 2014]. However, slabs that sink to stagnate at the base of the upper mantle do so typically by rolling back, and as such primarily induce toroidal flow (i.e., horizontal flow around their nearest edges) with relatively little potential for focused upwelling and decompression melting [*Piromallo et al*., 2006; *Long and Silver*, 2009]. For slab rollback, poloidal flow with upwelling in the backarc and near the tip of the slab is primarily important during the initial stages of rollback subduction [e.g., *Jadamec and Billen*, 2012], but declines as soon as the slab lies down to stagnate in the MTZ [*Faccenna et al*., 2010; *Strak and Schellart*, 2014].

As an alternative mechanism for upwelling and decompression melting above a stagnant slab, Richard and coworkers [*Richard and Bercovici*, 2009; *Richard and Iwamori*, 2010] have proposed convective instability of a buoyant hydrated layer directly overlying the slab. This mechanism has recently received increased attention, as seismic tomography has successfully imaged localized low-velocity anomalies that extend from the top of the slab to the base of the lithosphere, particularly beneath eastern Asia [*Lei and Zhao*, 2005; *Lei et al*., 2009; *Zhao et al*., 2009; *Lei et al*., 2013]. However, the thin hydrated layer, which results from sediment dehydration very close to the trench, is expected to become convectively stable before it reaches the MTZ (i.e. before $\sim$10 Myr, cf. *Goes et al*. [2011]) due to progressive cooling of the layer by the directly underlying (coolest part of the) slab. More favorable conditions for convective instability of a hydrated layer occur in the mantle wedge, i.e. before progressive cooling occurred [see *Gerya and Yuen*, 2003; *Gorczyk et al*., 2007]. Whereas geochemical signatures of basaltic volcanism formed above the mantle wedge indeed display evidence for subduction-related fluids in the source [*Iwamori*, 1991; *Wilson and Downes*, 2006], such evidence is often absent for volcanism above the stagnant slab [*Zou et al*., 2008].

Another mechanism for mantle upwelling from (or near) stagnant slabs and decompression melting has so far been largely ignored: convective instability of the slab itself. Though being cold and dense overall, a slab at the base of the upper mantle may become unstable, as its upper part is both thermally (cool) and compositionally (eclogite) denser than its underbelly (relatively warm harzburgite). Such instability may be advanced by slab-core superplasticity, which is a potential legacy of the slab's passage through the 410 km deep olivine-wadsleyite phase transition, where dynamic recrystallization is expected to causes significant grain-size reduction [*Vaughan and Coe*, 1981; *Rubie*, 1984; *Riedel and Karato*, 1997; *Yamazaki et al*., 2005]. The resulting microscale grain sizes may reduce the viscosity of the slab core by a couple of orders of magnitude in the deformation regime of diffusion creep [e.g., *Karato et al*., 2001].

In this study, we use two-dimensional numerical models of upper mantle convection to systematically explore buoyancy-driven instability of the stagnant slab's underbelly. We investigate the timescales of development of this instability, assess its potential to drive upwelling that persists through the entire upper mantle and to support sublithospheric melting, as well as discuss its consequences for the fate of slab materials. These predictions will help to distinguish this mechanism from alternative forms of upwelling.

2. Methods

In this study, we analyze a suite of two-dimensional models by numerically solving the equations for conservation of mass, momentum, and energy using the finite element code CITCOM [*Moresi et al*., 1996]. Our

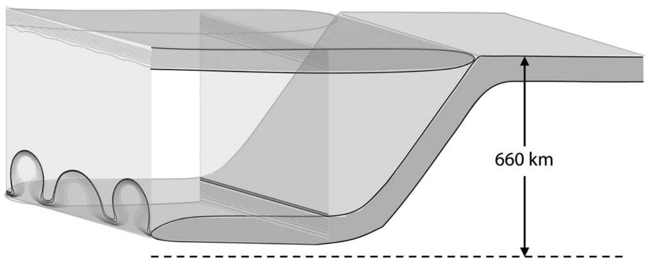

Figure 1. Conceptual three-dimensional visualization of convective instability rising out of a stagnant slab. The two-dimensional model represents a cross-section parallel to the trench. The distance of the model cross-section from the trench increases over time.

models are 1320 km wide, and 660 km deep, discretized by 1025 and 481 finite elements in the horizontal and vertical directions, respectively. Horizontally, grid spacing is uniform, but vertically, grid refinement allows improved resolution (of ~0.89 km) near the bottom of the computational box. All boundaries are closed to inflow and outflow. The thermal boundary conditions on both sides are reflective, while the top and bottom are held at a constant potential temperatures of $T_{top} = 0°C$ and $T_{bottom} = T_0 = 1350°C$ [*Herzberg et al.*, 2007].

The model is designed to investigate the behavior of a subducted slab that stagnates at the base of the upper mantle. The two-dimensional model represents a cross section that runs parallel to the trench of the subduction zone (i.e., the trench is out-of-plane of the two-dimensional model), and is fixed to the stagnant slab (Figure 1). Accordingly, distance of the model's cross section from the trench conceptually increases as model time increases (however, not necessarily proportionally, depending on subduction style). The fixture of the model to the slab, as well as expectation that convective instability both within the transition zone and at the base of the overriding lithosphere organize as longitudinal rolls in three dimensions [e.g., *Richter and Parsons*, 1975] motivate the choice of a simplified two-dimensional geometry (see Figure 2a for model setup). The initial thermal profile of the overriding plate corresponds to that of 5 Ma old oceanic lithosphere (i.e., according to the half-space cooling model), except for one test case as detailed in the text below.

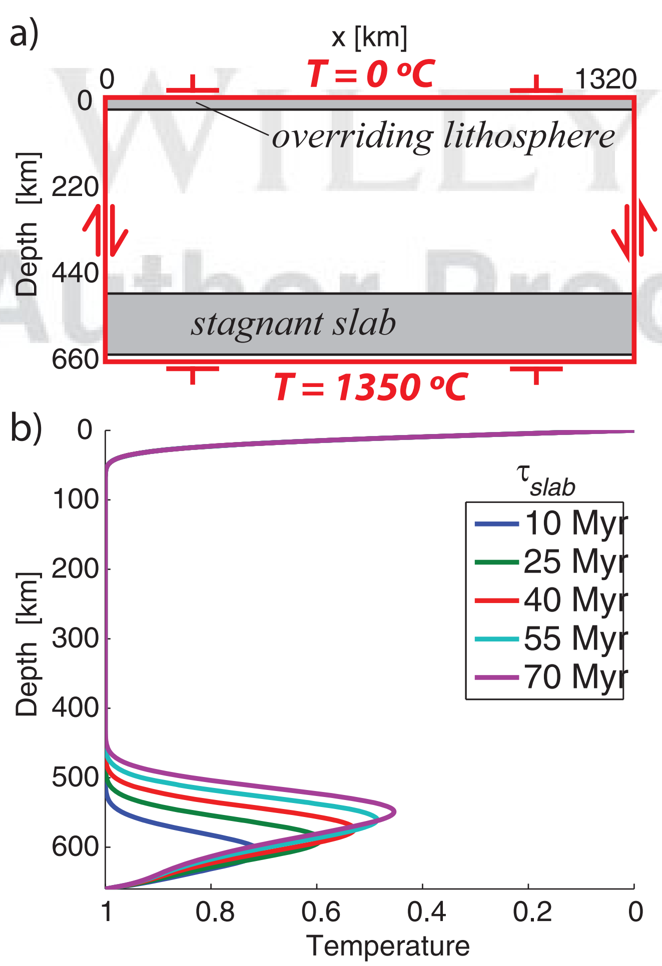

Figure 2. Initial and boundary conditions of our numerical models. (a) Thermal and velocity (free slip on the sides and no slip at the top and bottom) boundary conditions are marked red. The imposed thermal lithosphere and stagnant slab are denoted gray. The horizontally uniform initial thermal condition is detailed in Figure 2b as vertical profiles, which are a function of the age of the oceanic lithosphere (i.e., 5 Myr in all of our models) at the time of subduction τ_{slab}.

To determine the initial temperature profile of the subducted slab, we assume that the slab's thermal profile at the trench (i.e., just before subduction) corresponds to that of oceanic lithosphere of age τ_{slab}, and that it takes 10 Myr for the slab to sink to the base of the upper mantle

AGU Geochemistry, Geophysics, Geosystems 10.1002/2014GC005608

Table 1. Governing Parameters

Parameter	Description	Value; Range
E^*	Activation energy	120 kJ/mol
g	Gravitational acceleration	9.8 m/s
T_0	Reference temperature	1350°C
κ	Thermal diffusivity	$1 \cdot 10^6$ m^2/s
ρ_0	Reference density	3300 kg/m^3
A	Thermal expansivity	2.5×10^{-5} K^{-1} to 4.5×10^{-5} K^{-1} [a]
η_0	Reference viscosity	1.48×10^{19} Pa·s to 4.46×10^{19} Pa·s [a]
τ_{slab}	Plate age at trench	5–70 Ma [a]
$\Delta\rho_{ECL}$	Excess density of eclogite	91–150 kg/m^3 [b]
$\Delta\rho_F$	Density change due to depletion	-230 kg/m^3 to -100 kg/m^3 [b]

[a] Free parameter.
[b] Depth-dependent parameter (see text).

[cf. *Goes et al.*, 2011]. Further assuming that sinking occurs through an infinite space of $T = 1350$°C, we calculate the slab's thermal profile numerically using Fourier Series expansion. We then position the slab such that the 1282.5°C isotherm (i.e., the 0.95 isotherm nondimensionally) at the underbelly of the slab intersects the bottom boundary. Using the Crank-Nicholson scheme, we further allow the thermal profile to evolve (i.e., by diffusion) for another 1 Myr within the boundary conditions of the model (Figure 2b). The two-dimensional initial thermal conditions of the models are lateral extensions of these evolved profiles and further include a small thermal random noise (with amplitudes of ±15°C).

2.1. Rheology Parameterization

We use a Newtonian rheology with low activation energy ($E^* = 120$ kJ/mol; see Table 1 for notations) to model flow in the upper mantle in general, and in the MTZ in particular:

$$\eta = \eta_0 \exp\left(\frac{E^*}{RT} - \frac{E^*}{RT_0}\right), \tag{1}$$

where η_0 is the reference viscosity, R the ideal gas constant, T potential temperature, and T_0 the reference temperature.

The low value for E^* compared to experimental estimates for diffusion creep (~500 kJ/mol [*Karato and Wu*, 1993]) has been chosen to simulate the complex rheology of the upper mantle and transition zone. For example, *Christensen* [1984] has shown that convection of a non-Newtonian liquid can be mimicked by using a Newtonian rheology with an E^* that is reduced by a factor of 2–3. Observations of seismic anisotropy in the MTZ and much of the upper mantle indicate that non-Newtonian dislocation creep is a dominant deformation mechanism [e.g., *Yuan and Beghein*, 2014], consistent with mineral-physics constraints [e.g., *Karato and Wu*, 1993; *Shimojuku et al.*, 2009]. As an additional complication, micrometer-scale grain sizes are thought to be present in the cool slab core due to dynamic recrystallization of wadsleyite as the slab crosses the 410 km discontinuity [*Riedel and Karato*, 1997; *Karato et al.*, 2001] and slow grain growth [*Yamazaki et al.*, 2005]. Such small grain sizes have been proposed to reduce slab viscosity by orders of magnitude in the deformation regime of diffusion creep to render the cool slab core less viscous than the warm ambient mantle ("superplasticity"). Thus, cold temperatures may be associated with the lowest viscosities in the MTZ, something that is consistent with even a negative effective E^*. In our choice of E^*, however, we do not explicitly account for superplasticity of the slab core. Accordingly, this choice remains a conservative estimate.

2.2. Density Parameterization

Mantle buoyancy drives the flow and is affected by thermal and compositional density anomalies. We take mantle density ρ to be dependent on temperature, depletion of the peridotite matrix F, and the volume fraction of eclogite X_{ECL}:

$$\rho = \rho_0 - \alpha(T - T_0) + F\Delta\rho_F + X_{ECL}\Delta\rho_{ECL}, \tag{2}$$

where ρ_0 is reference density, α is thermal expansivity, $\Delta\rho_F$ is the density change due to depletion, and $\Delta\rho_{ECL}$ is the excess density of eclogite. Parameters $\Delta\rho_{ECL}$ and $\Delta\rho_F$ are depth-dependent (parameterized according to *Xu et al.* [2008]). At depths <300 km, $\Delta\rho_{ECL}$ and $\Delta\rho_F$ are set to 150 and -165 km/m^3; between 300 and 410 km, they are fixed at 210 and -230 km/m^3; and deeper than 410 km, they are 91 and -100 km/m^3, respectively.

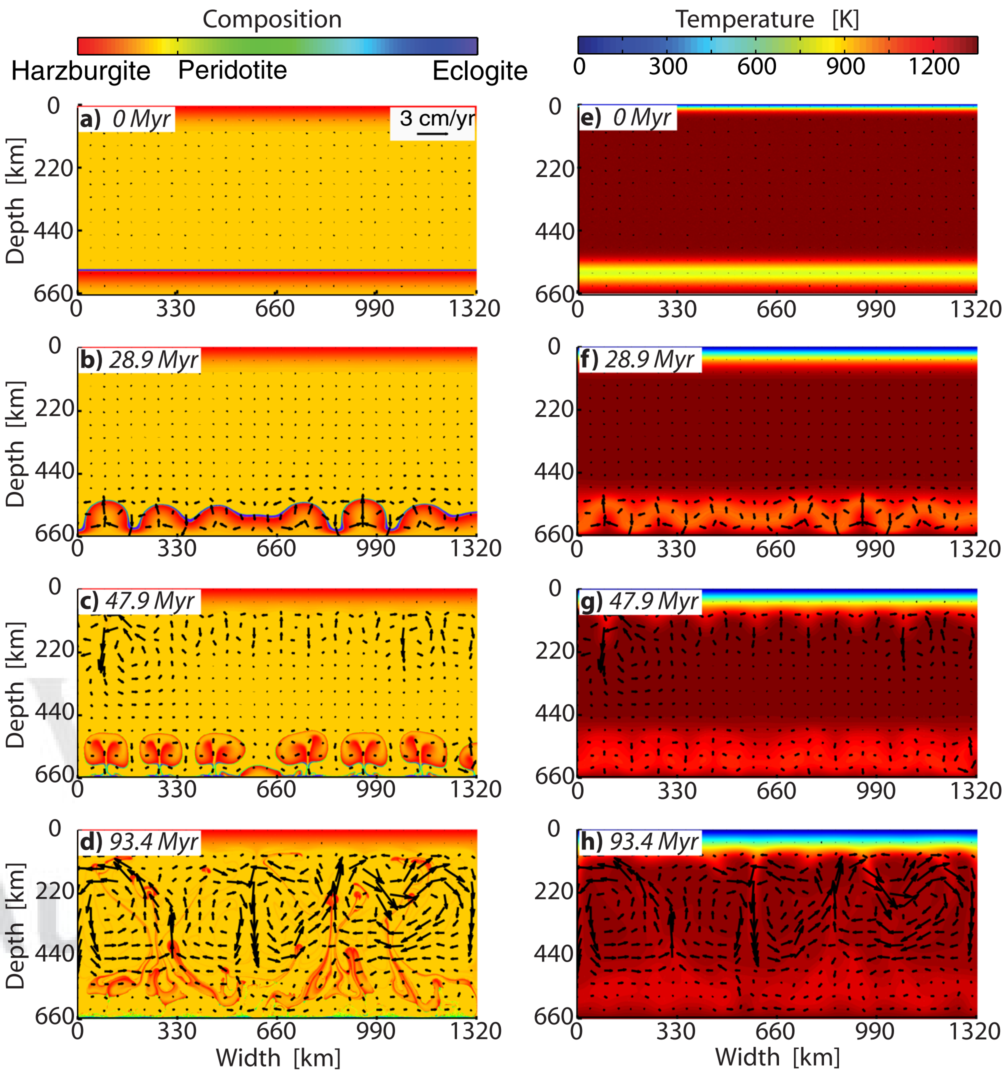

Figure 3. Time evolution (i.e., from top to bottom) of model results for reference case 13/E. (left column; a–d) Composition (colors) and velocity (arrows); (right column; e–h) Temperature (°C). Arrow length scale is the same in all plots (see Figure 3a).

3. Results

3.1. General Model Predictions

Figure 2b shows the initial thermal condition of the model as a one-dimensional vertical profile with a thin top thermal boundary layer and a cool stagnant slab at the base of the model. We account for warming of the slab during its passage through the upper mantle before the onset of the simulation. However, the slab's core is cool compared to the ambient mantle, and hence anomalously dense. A thin but dense layer of eclogite (i.e., the high-pressure polymorph of the basaltic oceanic crust) atop the slab further increases this density anomaly (Figure 3a). The effects of temperature and eclogite on density are somewhat offset by those of buoyant harzburgite within the slab. Harzburgite is the depleted residuum of previous mid-ocean ridge melting, with depletion ranging from ~20% just beneath the eclogite layer and steadily decreasing with depth (Figure 3a). As thermal effects are dominant, however, the underbelly of the slab is buoyant compared to the slab's core. Thus, the stagnant slab is potentially convectively unstable.

The evolution of density and viscosity over time controls the behavior of the slab. Although the slab initially displays an unstable density configuration, convection does not immediately develop as being impeded by the high viscosity of the slab. We find that heating the cool slab by the ambient mantle from below and above ultimately drives convective instability. The most important consequence of conductive slab heating is that the viscosity of the slab's core decreases and thus the local Rayleigh number increases with time. In addition, the warm and less dense layer of mantle at the underbelly of the slab continuously grows (as the modeled mantle is heated from below), pushing up on the slab. Both effects eventually render convection a more efficient mode of heat transport than conduction. Consequently, convective instabilities rise out of the warm layer at the slab's underbelly at a given onset age (see also Appendix A).

Bottom heating, however, is not critical for convective instability to occur, as is demonstrated by an (albeit unrealistic) test-case with reflective bottom thermal boundary conditions (i.e., zero heat flow from the lower mantle to the base of the slab). In this test case, instability rising out of the slab is less vigorous and somewhat delayed (by 5$\sim$10 Myr) than in a similar case with bottom heating (i.e., case 13/E), but both cases are analogous in general characteristics.

Convective instability eventually causes disintegration of the slab. As the warm mantle below pushes through the slab (Figure 3b), the instabilities start to form plume-like upwellings. These upwellings displace the dense veneer of eclogite to the side (ultimately, most eclogite accumulates near the bottom boundary of the model; Figure 3d). Most of the buoyant harzburgite is instead entrained by the plumes (Figure 3c). The plumes rise somewhat above the original depth of the top of the slab, but do not penetrate much further through the warmer (and therefore less dense) part of the upper mantle (Figures 3c and 3g). As the plumes are cooler than the ambient mantle, the positive compositional buoyancy of the entrained harzburgite is at first insufficient to sustain plume ascent all the way to the base of the lithosphere. Accordingly, convection is at first mostly restricted to the deep upper mantle.

In our models, passive mantle flow related to small-scale sublithospheric convection (SSC) ultimately drives further ascent of materials that originate from the slab. As the overriding lithosphere is cooled from above, the cool sublithospheric mantle slowly thickens. As soon as it reaches a critical layer thickness, the sublithospheric mantle undergoes instability to drive SSC in the asthenosphere (Figure 3c). SSC cells readily break down into the lower upper mantle [*Korenaga and Jordan*, 2004] (Figure 3d). By this time, the slab-derived upwellings have lost most of their negative thermal buoyancy due to thermal dissipation (i.e., diffusion). SSC stirs up slab material and transports harzburgite to the base of the lithosphere. To minimize any interaction between SSC and the instability rising out of the slab, we tune our models such that the former develops much later than the latter (initial age of the overriding plate of only 5 Ma delays SSC). However, in nature both processes are expected to occur coevally in order to allow upwellings to ascend more quickly through the entire upper mantle and to the base of the lithosphere, as is demonstrated by a test case with an initial age of the overriding plate of 70 Myr (i.e. close to the critical age for onset of SSC). In this test case, slab-derived upwellings reach the base of the lithosphere $\sim$5 Myr sooner than in a similar case (i.e., case K; see Table 2). T2

3.2. Parameter Study

We vary key model parameters to study their effects on the onset time τ_{onset} and wavelength of convective instability of the slab λ (Table 2). The parameters we investigate are the slab age at trench, which defines the thermal structure of the subducted slab (Figure 2b), mantle viscosity, and thermal expansivity (Tables 1 and 2). Mantle viscosity controls both thermal and compositional convection, whereas thermal expansivity affects thermal convection only. We use the root mean square (RMS) of the vertical velocity component at a depth of 606 km ($v_{rms,606}$) to define a criterion for τ_{onset}. At τ_{onset}, $v_{rms,606}$ reaches and surpasses $0.05(v_{max,606} - v_{start,606}) + v_{start,606}$ for the first time, where $v_{start,606}$ and $v_{max,606}$ are the initial and maximum RMS vertical velocity measured. Time evolution of $v_{rms,606}$ for select parameter suites are shown in Figure 4. F4

We find that model results strongly depend on the slab age at trench τ_{slab}. As the effective thermal age of oceanic plates is limited by SSC to $\sim$70 Ma [e.g., *Doin and Fleitout*, 1996], we explore τ_{slab} in the range of 5 and 70 Ma (Cases A–O in Table 2), keeping all other parameters fixed. τ_{slab} defines the initial condition of the model (Figure 2b). Old plates have developed a thicker thermal boundary layer than young plates as they are subducted, and hence sustain a thicker and cooler thermal anomaly as they enter the MTZ. For such old and thick plates, the slab's eclogite layer (i.e., formerly oceanic crust) is also initially positioned shallower. The net effect of these differences in initial condition as a function of τ_{slab} is that τ_{onset} and λ generally increase with increasing τ_{slab} (In contrast, peak plume rise speeds do not show a clear trend with τ_{slab}; see peaks of curves in Figures 4a and 4b). The key parameter controlling λ is the thickness of the layer that goes unstable (i.e., the slab and its underbelly). In contrast, key to control τ_{onset} is the initial temperature minimum of the slab's core, which defines the effective viscosity of the slab. The increase of τ_{onset} with τ_{slab}

AGU Geochemistry, Geophysics, Geosystems 10.1002/2014GC005608

Table 2. List of Key Model Parameters and Key Model Predictions for All Our Cases (Except for Test-Cases as Detailed in the Text)

	Case	τ_{slab} (Ma)	η_0 (Pa·s)	α (K^{-1})	τ_{onset} (Myr)	$v_{max,606}$ (cm/yr)	λ (km)
Plate age at trench	A	5	2.98×10^{19}	3.5×10^{-5}	8.15	0.76	113
	B* (5)	10	2.98×10^{19}	3.5×10^{-5}	10.79	0.86	120
	C	15	2.98×10^{19}	3.5×10^{-5}	14.07	0.84	140
	D	20	2.98×10^{19}	3.5×10^{-5}	18.59	0.88	145
	E* (13, γ)	25	2.98×10^{19}	3.5×10^{-5}	20.45	0.86	159
	F	30	2.98×10^{19}	3.5×10^{-5}	25.70	0.77	162
	G	35	2.98×10^{19}	3.5×10^{-5}	23.43	0.90	181
	H	40	2.98×10^{19}	3.5×10^{-5}	27.66	0.93	180
	J	45	2.98×10^{19}	3.5×10^{-5}	32.23	0.95	207
	K	50	2.98×10^{19}	3.5×10^{-5}	31.05	0.87	186
	L* (III)	55	2.98×10^{19}	3.5×10^{-5}	34.80	0.99	215
	M	60	2.98×10^{19}	3.5×10^{-5}	39.89	1.02	223
	N	65	2.98×10^{19}	3.5×10^{-5}	35.34	0.97	250
	O* (21)	70	2.98×10^{19}	3.5×10^{-5}	33.21	0.99	266
Reference viscosity	1	10	1.48×10^{19}	3.5×10^{-5}	5.84	1.41	119
	2	10	1.99×10^{19}	3.5×10^{-5}	6.88	1.23	120
	3	10	2.23×10^{19}	3.5×10^{-5}	8.38	1.05	120
	4	10	2.55×10^{19}	3.5×10^{-5}	9.45	0.95	120
	5* (B)	10	2.98×10^{19}	3.5×10^{-5}	10.79	0.86	120
	6	10	3.57×10^{19}	3.5×10^{-5}	12.53	0.76	121
	7	10	4.46×10^{19}	3.5×10^{-5}	15.03	0.65	137
	8	25	1.48×10^{19}	3.5×10^{-5}	11.55	1.50	158
	9	25	1.79×10^{19}	3.5×10^{-5}	13.53	1.31	159
	10	25	1.99×10^{19}	3.5×10^{-5}	14.83	1.19	159
	11	25	2.23×10^{19}	3.5×10^{-5}	16.38	1.09	158
	12	25	2.55×10^{19}	3.5×10^{-5}	18.20	0.98	144
	13* (E, γ)	25	2.98×10^{19}	3.5×10^{-5}	20.45	0.86	145
	14	25	3.57×10^{19}	3.5×10^{-5}	23.46	0.76	149
	15	25	4.46×10^{19}	3.5×10^{-5}	27.56	0.65	145
	16	75	1.48×10^{19}	3.5×10^{-5}	21.04	1.85	249
	17	75	1.79×10^{19}	3.5×10^{-5}	24.04	1.6	248
	18	75	1.99×10^{19}	3.5×10^{-5}	25.95	1.46	254
	19	75	2.23×10^{19}	3.5×10^{-5}	28.46	1.31	256
	20	75	2.55×10^{19}	3.5×10^{-5}	32.49	1.19	258
	21* (O)	75	2.98×10^{19}	3.5×10^{-5}	37.20	1.09	257
	22	75	3.57×10^{19}	3.5×10^{-5}	43.74	0.96	255
	23	75	4.46×10^{19}	3.5×10^{-5}	51.77	0.79	254
α	I	55	2.98×10^{19}	2.5×10^{-5}	31.00	0.95	214
	II	55	2.98×10^{19}	3.0×10^{-5}	33.60	0.98	215
	III* (L)	55	2.98×10^{19}	3.5×10^{-5}	34.80	0.99	215
	IV	55	2.98×10^{19}	4.0×10^{-5}	36.15	1.02	217
	V	55	2.98×10^{19}	4.5×10^{-5}	37.71	1.03	218
Fracture zone	α	25, 15	2.98×10^{19}	3.5×10^{-5}	9.33	0.44	189
	β	25, 20	2.98×10^{19}	3.5×10^{-5}	11.98	0.69	201
	γ* (13,E)	25, 25	2.98×10^{19}	3.5×10^{-5}	20.48	0.86	159
	δ	25, 27	2.98×10^{19}	3.5×10^{-5}	14.92	0.74	179
	ε	25, 30	2.98×10^{19}	3.5×10^{-5}	12.43	0.68	213
	ζ	25, 35	2.98×10^{19}	3.5×10^{-5}	11.35	0.57	213

[a]Case identifiers are given in the second column, parameters varied between cases of one suite in the first column. (*) A subset of cases are listed more than once; the equivalent case identifier(s) are reported in parentheses. For determination of onset ages τ_{onset} and maximum amplitudes $v_{max,606}$ of convective instability, see text (section 3.2). Wavelengths λ are determined at τ_{onset} as the weighted average of the three most dominant wavelengths of the vertical velocities at 606 km depth. We choose to consider the three most dominant wavelengths as the box width is often not a multiple of the preferred wavelength.

agrees well with the predictions of a semianalytical solution (see Appendix A). However, τ_{onset} only steadily increases with τ_{slab} at low τ_{slab}, but not at high $\tau_{slab} > 50$ Myr. For high τ_{slab}, τ_{onset} rather tends to scatter around 50 Myr (Figure 4b). This scattering is due to a limitation in terms of permitted λ in a model box of finite width. Convective instability is artificially delayed as long as its preferred wavelength is not exactly a natural fraction of twice the model box width (see Appendix A).

Another key parameter is reference mantle viscosity η_0. η_0 is a source of great uncertainty for our understanding of mantle dynamics, both due to the lack of good constraints for this parameter and due to its huge influence on the mobility of mantle rocks. Along these lines, we run three suites of calculations varying η_0 between 1.48×10^{19} and 4.46×10^{19} Pa·s; each suite uses a constant value of τ_{slab} of 10, 25, or 75

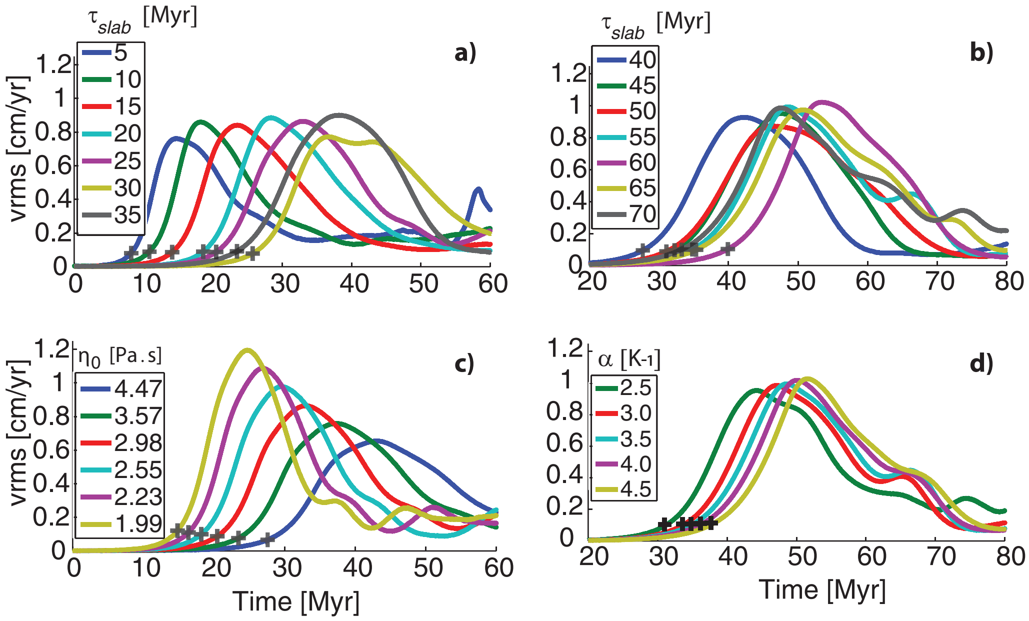

Figure 4. Vigor of convective instability over time. For four parameter suites (see legends), colored curves show the time evolution of $v_{rms,606}$ (i.e., the root mean square of the vertical velocity component at 606 km depth). Typical plume rise speeds are proportional to $v_{rms,606}$. Cases shown are (a) A–G, (b) H–O, (c) 10–15, and (d) I–V. Black crosses mark the onset times picked for each case.

Ma and all other parameters are fixed (Cases 1–23 in Table 2). We find that τ_{onset} systematically increases with increasing η_0 (Figure 4c). Furthermore, λ as well as peak plume rise speeds steadily decrease with increasing η_0 in our models.

In contrast to the controlling parameters τ_{slab} and η_0, we find that thermal expansivity does not appreciably affect convective instability. We vary thermal expansivity α between 2.5×10^{-5} and 4.5×10^{-5} K^{-1}, while keeping all other parameters fixed (Cases I–VI in Table 2). We find that onset ages (as well as peak plume rise speeds) increase with increasing α, albeit just within a narrow range of about 31–38 Myr (and 1.95–2.15 cm/yr). While these findings generally confirm the important role of thermal buoyancy in driving convective instability of the slab, they also document the secondary role of α within the experimental uncertainties for this parameter [*Inoue et al.*, 2004; *Katsura et al.*, 2004; *Ye et al.*, 2012].

3.3. The Effects of Heterogeneity

We also explore the effects of lateral density heterogeneity on convective instability of a stagnant slab. As an example for density heterogeneity, we model a subducted fracture zone by juxtaposing two slab segments with different τ_{slab} (Figure 5a). The subducted fracture zone is positioned near the center of the computational box (i.e., at $x = 742.5$ km). The initial thermal condition, however, does not just involve a simple step function at the fracture zone; the transition between the two sides of the slab is rather smoothed linearly over 66 km (i.e., 5% of the width of the box). We note that the old slab segment is initially thicker and denser than the young segment. Thus, the slab's coolest core is initially positioned shallower on the old side than on the young side. This is a direct consequence of our initial thermal condition, for which the depth of the temperature minimum decreases with increasing τ_{slab} (see Figure 2b), and generally consistent with isostatic compensation of slab segments of different thickness by the phase change at 660 km depth. F5

The consequence of this initial condition is that the cooler and denser old slab segment tends to slowly sink as a whole to establish equilibrium between the two sides. This initial disequilibrium drives box-wide clockwise rotation, an artifact of our model setup that causes nonzero $v_{start,606}$ for all fracture-zone models. Beyond this artifact, we observe that instabilities develop sooner and with a larger vigor in cases with than in cases without a fracture zone. Onset ages systematically decrease with the age difference between the two sides of the slab, and thus with the amplitude of initial heterogeneity. The first plumes form near the fracture zone on the young slab segment (Figures 5a and 5b). About 15 Myrs thereafter, plumes develop all over the young segment (Figure 5c), and ultimately also on the old slab segment (not shown).

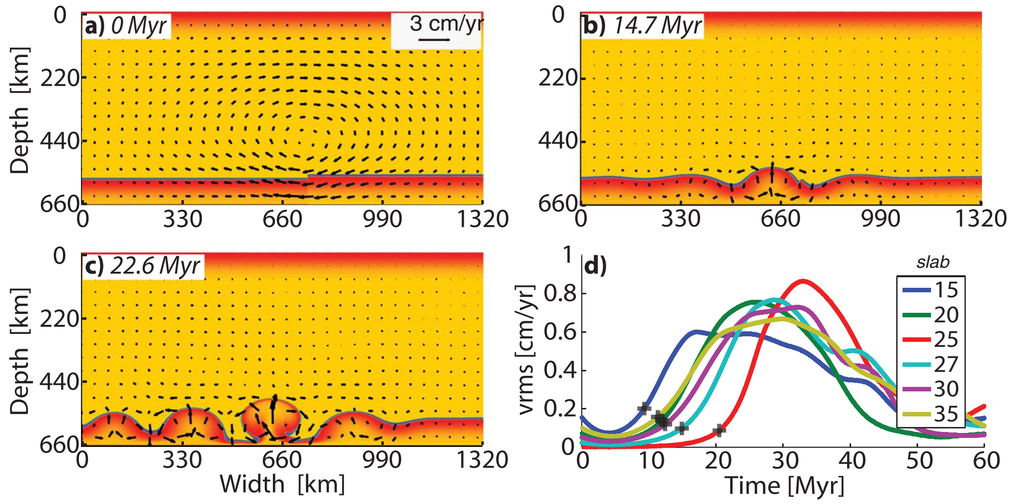

Figure 5. Convective instability rising out of a heterogenous slab. For case ζ, snapshots of composition and velocity at (a) 0 Myr, (b) 14.7 Myr, and (c) 22.6 Myr. Arrow length scale is the same in all plots (see Figure 5a). τ_{slab} is 25 Ma for the left slab segment and 35 Ma for the right segment. The color scale for composition is the same as Figure 3. Analogous to Figure 4, Figure 5d shows the time evolution of $v_{rms,606}$ for a suite of cases with τ_{slab} varied for one slab segment (see legend) and fixed at 25 Ma for the other segment (i.e., for cases α-ζ). Black crosses mark onset times.

4. Discussion

We find in our numerical models that slabs which stagnate in the MTZ can go convectively unstable to spawn plume-like upwellings that rise out of the warm underbelly of the slab. Convection is at first limited to within the deep upper mantle, but upwellings are eventually entrained by ambient-mantle flow to reach the base of the overriding lithosphere. For a range of parameters, we find timescales for the onset of the instability of tens of million years. Onset ages are primarily controlled by (and increase with increasing) slab-core viscosity, which itself is a function of MTZ rheology and the age of the subducted slab (see also Appendix A). Since we neglect the effects of grain-size reduction that is thought to occur as the slab enters the MTZ; however, slab-core viscosities as well as onset ages of convective instability are most likely overestimates [*Vaughan and Coe*, 1981; *Rubie*, 1984; *Riedel and Karato*, 1997; *Karato et al.*, 2001; *Yamazaki et al.*, 2005]. Future efforts to constrain onset ages, perhaps by seismic illumination of the shape of the slab's eclogite layer that gets unstable, may improve our understanding of MTZ rheology.

We also find that heterogeneity within the slab, such as subducted fracture zones, reduces onset ages. Similarly, any thermal or compositional variations beneath the slab are expected to promote convective instability. Instability is expected to be even more so promoted along the edges of the stagnant slab, where arguably the strongest lateral density heterogeneity in the MTZ occurs (i.e., slab versus no slab). These predictions are analogous to previous findings for top-down driven small-scale convective instability (SSC), which can be triggered by the presence of heterogeneity such as fracture zones [*Huang et al.*, 2003; *Dumoulin et al.*, 2005], and even more so along larger steps of lithospheric thickness (i.e., a variant of SSC that has been dubbed edge-driven convection [*King and Anderson*, 1998; *King and Ritsema*, 2000]). Along these lines, we hypothesize the first and most vigorous upwellings to rise adjacent to the stagnant slab's toe as well as through slab gaps.

Once the upwellings reach the base of the lithosphere, they potentially undergo decompression melting to sustain intraplate volcanism at a given distance inland from the trench. As our models predict upwellings to be somewhat cooler than the ambient mantle, however, any such decompression melting would have to be sustained by compositional (i.e., fertile) anomalies. Candidate fertile lithologies involve eclogite and hydrated peridotite. Dense eclogite originating from the top of the slab (i.e., formerly oceanic crust) is indeed predicted to be entrained by upwelling plumes to reach the base of the lithosphere, albeit to small extents on the order of ∼0.1% only (Figure 6). A layer of hydrated peridotite atop the eclogite layer (which originally formed close to the trench due to dehydration of subducted sediments) is an alternative fertile source lithology. While this layer is expected to become convectively unstable before the slab reaches the

AGU Geochemistry, Geophysics, Geosystems 10.1002/2014GC005608

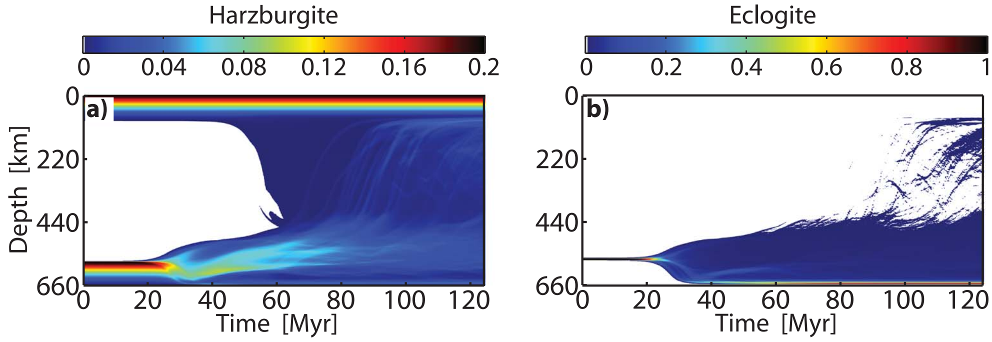

Figure 6. Evolution of the average volume fraction of (a) harzburgite and (b) eclogite with depth for case 13/E. The cutoff at the lower end of the colorscales (blue versus white) is at 0.01%.

MTZ [*Gerya and Yuen*, 2003; *Gorczyk et al.*, 2007], some hydrated peridotite may survive the passage through the upper mantle and be passively entrained by convective instability rising out of the slab.

Along these lines, geochemical signatures of associated intraplate volcanism should be controlled by mantle melting of eclogite and perhaps hydrated peridotite, in addition to continental contamination. A signature of eclogite melting has indeed been identified for intraplate lavas in eastern China [*Sakuyama et al.*, 2013]. A contribution from melting the relatively dry peridotite matrix is only expected as long as upwellings are warmer than, or at least as warm as, the ambient mantle. This requirement may be met by upwellings rising through slab windows or adjacent to slab toes (not explicitly modeled here), which should be warmer than those rising out of the slab's underbelly, particularly for a superadiabatic lower mantle. Somewhat higher potential temperatures in the lower than in the upper mantle may be the consequence of long-term moderated mass transfer across the MTZ [e.g., *Christensen*, 1995], a situation for which slab stagnation itself provides some good evidence. Future models of slab-derived upwellings should indeed include melting parameterizations for various lithologies.

Decompression melting induced by slab-derived upwellings can provide an explanation for intraplate volcanism in Europe, eastern China, and western North America. These regions display volcanic activity and are underlain by slabs that stagnate in the MTZ. Volcanism is usually relative low-volume and somewhat sporadic, as is consistent with the low extents of fertile lithologies transported to the base of the lithosphere by slab-derived upwelling (cf. Figure 6b). Volcanoes typically form about 1000–2000 km away from the trench, a distance that implies timescales for convective instability rising out of the slab of about 15–30 Myr, i.e., quite a bit smaller than those predicted by our models without heterogeneity (and with simplified rheology). However, volcanoes are commonly underlain by a slab window (e.g., Changbaishan) or close to the slab toe (e.g., Datong, western US volcanism [www.navdat.org], Eifel, Auvergne) [*Faccenna et al.*, 2010; *Lei et al.*, 2013]. Such settings provide lateral heterogeneity much larger than that across a fracture zone, and are thus expected to allow for vigorous slab-derived upwellings with a significantly earlier onset ages (cf. section 3.3). Intraplate volcanism in Europe and China has often been associated to plumes/upwellings that rise from a thermal boundary layer in the mid mantle [*Lustrino and Wilson*, 2007; *Lei et al.*, 2013]. Our work implies that this thermal boundary layer may in fact be positioned at the underside of the slab.

In contrast to individual plume-like upwellings ascending through slab gaps or along slab toes, convective instability rising out of the slab's underbelly potentially disrupts the slab's integrity. According to our models, this disruption would occur quite a bit later than the rise of these first individual upwellings. Potential consequences involve eradication of the slab's compositional stratification as well as impairment of slab seismic visibility. For example, our reference case 13/E predicts the slab's compositional stratification to be distorted starting at $\sim$30 Myrs (Figure 3e). As convection is mostly restricted to the deep upper mantle, however, the slab's overall thermal structure remains coherent until 50–90 Myrs (Figures 3f and 3h). Accordingly, a slab that undergoes instability should soon appear blurred in seismic images, but continue to appear as one whole anomaly for relatively long timescales, consistent with observations [*van der Meer et al.*, 2010]. Persistent slab seismic visibility may perhaps further be advanced by an eventual slowdown or even shutdown of convective instability due to an increase of slab viscosity. Such an increase could be sustained by grain growth within the stagnant slab (albeit inferred to be slow [*Yamazaki et al.*, 2005]), or an entering of the slab into the lower mantle. On the other hand, our results suggest the intriguing possibility of complete stagnant slab disintegration (and seismic invisibility) on long timescales, the rheological conditions for which are yet to be constrained by observations.

The disruption of the integrity of the slab by convective instability further acts to separate eclogite from harzburgite, and thus has important long-term consequences for the compositions of the upper and lower mantles. As shown in Figure 6, our models predict harzburgite to be ultimately mixed in with the upper mantle, whereas they predict eclogite to accumulate at the bottom of the MTZ (i.e., the bottom of the box). In nature, an eclogitic layer at the bottom of the MTZ may be supported by a density crossover between eclogite and ambient-mantle materials in the uppermost lower mantle [*Hirose et al*., 1999], where eclogite becomes buoyant. In the long-term, however, eclogite accumulations at ~660 km depth are expected to enter the lower mantle despite this support (e.g., due to entrainment), particularly once they reach a layer thickness similar to that of the depth range, over which the density overturn occurs (i.e., ~80 km). Along these lines, convective instability of stagnant slabs can act to filter mantle heterogeneity in order to sustain a compositional difference between a somewhat more harzburgitic upper mantle and a somewhat more "eclogitic" lower mantle (accounting for the relevant phase transitions i.e., a dominantly perovskitic lower mantle) over large geologic timescales. Such a difference has indeed been proposed based on comparison of geophysical constraints with mineral-physics estimates of lower-mantle rock properties [e.g., *Cobden et al*., 2009; *Murakami et al*., 2012]. A perovskitic lower mantle may further reconcile chondrite models for bulk-Earth compositions. Understanding the separation of eclogite and harzburgite within stagnant slabs is vital to constrain heat and material fluxes through the mantle.

5. Conclusions

To study the origin of intraplate volcanism, we explore the behavior of stagnant slabs in the MTZ. We show that weak slabs that stagnate in the MTZ can go convectively unstable within tens of Myr, or less. Upwellings rising out of the slab's underbelly are relatively cool and thus do not actively rise through the upper mantle at first, but are ultimately entrained by ambient-mantle flow to reach the base of the lithosphere and undergo decompression melting. The soonest, warmest, and most vigorous upwellings are likely to rise along slab edges, and adjacent to heterogeneity within or below the slab. They entrain a small fraction of fertile eclogite and may thus be subject to decompression melting. Continental intraplate volcanism indeed often occurs above stagnant slabs, particularly above slab toes or slab windows. We further show that convective instability of a stagnant slab can result in slab disintegration and separation of harzburgite from eclogite with the destinations of these materials the upper and lower mantles, respectively. Such a separation may sustain a compositional gradient across the MTZ over large geologic timescales, perhaps over billions of years.

Appendix A

To benchmark the results of our numerical experiments, we compare model onset ages with a semianalytical solution. We estimate semianalytical onset ages by computing local thermal Rayleigh numbers Ra_{loc} of the layer that potentially goes convectively unstable. This layer of unstable thermal stratification ranges from 660 km depth to the core of the slab, where the temperature minimum occurs (Figure 2b). As the slab gets heated from below and above, Ra_{loc} evolves. We compute thermal evolution of the slab numerically using Fourier series expansion. The thickness of the layer of unstable stratification h, the temperature difference across it, as well as the relevant viscosity at the top of the layer η_{loc} evolve with time and thus control evolution of Ra_{loc}:

$$Ra_{loc}=\frac{\alpha(T_0-T_{loc})\rho_0 g h^3}{\kappa\eta_{loc}}, \tag{A1}$$

where T_{loc} is the minimum temperature of the slab. η_{loc} is calculated from T_{loc} and equation (1).

In solving equation (A1), we find that T_{loc} as well as h monotonically increase, and η_{loc} monotonically decreases with time. As the decrease of η_{loc} (i.e., a function of T_{loc}) is much stronger than the increase of T_{loc} (see equation (1)), the net effect is that Ra_{loc} monotonically increases with time. As soon as Ra_{loc} exceeds a

AGU Geochemistry, Geophysics, Geosystems 10.1002/2014GC005608

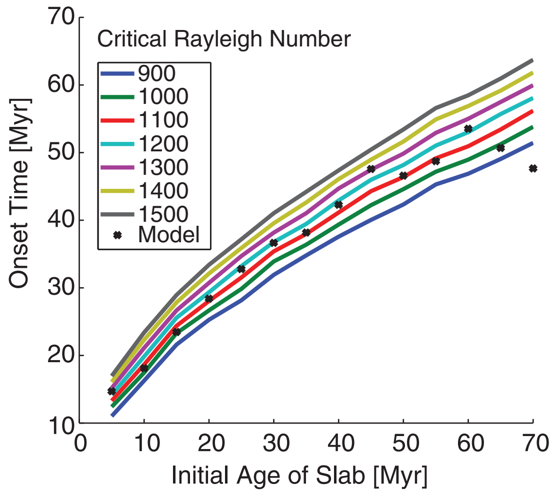

Figure A1. Comparison of semianalytically estimated onset ages as a function of slab age at trench with predictions from the two-dimensional numerical experiments. Crosses are numerical model results; colored curves are semianalytical predictions for different critical Rayleigh numbers. Reference viscosity is fixed at 2.98×10^{19} Pa·s.

critical Rayleigh number Ra_{crit}, convection becomes a more efficient mode of heat transfer than conduction, and convective instability develops. The time t_{onset}, after which $Ra_{loc} > Ra_{crit}$, is a function of the model parameters and initial thermal conditions. Initial thermal conditions primarily depend on the slab age at trench τ_{slab} (Figure 2b). Ra_{crit} is usually $\sim$1000, but its exact value depends on the aspect ratio λ/h of the convective cell [e.g., *Turcotte and Schubert*, 1982], where λ is the wavelength of convective instability.

Our semianalytical solution predicts that t_{onset} increases as a function of τ_{slab} (Figure A1). This increase is first and foremost due to an increase of η_{loc} with increasing τ_{slab}. Older slabs are cooler and hence more viscous at any given time in the experiment. For example at $t = 0$, η_{loc} equals $\sim 8\eta_0$, $\sim 110\eta_0$ and $\sim 1900\eta_0$ at $\tau_{slab} = 5$ Ma, $\tau_{slab} = 25$ Ma and $\tau_{slab} = 70$ Ma, respectively. The rate of the increase of t_{onset} with τ_{slab} somewhat decreases at high τ_{slab}.

The general trend of t_{onset} as a function of τ_{slab} as well as the absolute values of t_{onset} agree well with the results of our numerical experiments (lines versus crosses in Figure A1). As we do not take into account the effects of composition in calculating Ra_{loc}, this good agreement suggests that unstable thermal density stratification critically drives convective instability in our numerical experiments. That compositional buoyancy is only marginally important to drive instability is explained by a trade-off between the effects of harzburgite and basalt on total buoyancy of the top of the slab. In particular, our analysis shows that slab softening due to heating from below and above is key for triggering instability.

Any scatter of the numerical predictions in terms of onset age about each of the semianalytical solutions (e.g., for $Ra_{crit} = 1100$: scatter of crosses about red line in Figure A1) is well explained by limitations for permitted λ in finite computational domains. In the numerical experiments, only natural fractions of twice the box width are permitted for λ. In particular for high τ_{slab}, for which the preferred λ is of the same order as box width, a mismatch between preferred and permitted λ is likely to affect onset ages. Therefore, we expect that using box width much larger than those modeled further improves the match between numerical model predictions and the semianalytical solution.

Acknowledgments
We thank Guillaume Richard, an anonymous reviewer and the editor for their thoughtful and detailed comments that helped to improve the manuscript. This study has been supported by NSF grant EAR-1141938. A basic version of the software that was used to run the numerical models (see Methods section) is available at Computational Infrastructure for Geodynamics (http://www.geodynamics.org).

References

Ballmer, M. D., J. van Hunen, G. Ito, P. J. Tackley, and T. A. Bianco (2007), Non-hotspot volcano chains originating from small-scale sublithospheric convection, *Geophys. Res. Lett.*, *34*, L23310, doi:10.1029/2007GL031636.

Ballmer, M. D., J. van Hunen, G. Ito, T. A. Bianco, and P. J. Tackley (2009), Intraplate volcanism with complex age-distance patterns: A case for small-scale sublithospheric convection, *Geochem. Geophys. Geosyst.*, *10*, Q06015, doi:10.1029/2009GC002386.

Ballmer, M. D., G. Ito, J. van Hunen, and P. J. Tackley (2010), Small-scale sublithospheric convection reconciles geochemistry and geochronology of 'Superplume' volcanism in the western and south Pacific, *Earth Plant. Sci. Lett.*, *290*(1-2), 224–232.

Ballmer, M. D., C. P. Conrad, E. I. Smith, and N. Harmon (2013a), Non-hotspot volcano chains produced by migration of shear-driven upwelling toward the East Pacific Rise, *Geology*, *41*(4), 479–482.

Ballmer, M. D., G. Ito, C. J. Wolfe, and S. C. Solomon (2013b), Double layering of a thermochemical plume in the upper mantle beneath Hawaii, *Earth Planet. Sci. Lett.*, *376*, 155–164.

Bianco, T. A., C. P. Conrad, and E. I. Smith (2011), Time dependence of intraplate volcanism caused by shear-driven upwelling of low-viscosity regions within the asthenosphere, *J. Geophys. Res.*, *116*, B11103, doi:10.1029/2011JB008270.

Bonatti, E., and C. G. A. Harrison (1976), Hot Lines in the Earths Mantle, *Nature*, *263*(5576), 402–404.

Buck, W. R., and E. M. Parmentier (1986), Convection beneath young oceanic lithosphere: Implications for thermal structure and gravity, *J. Geophys. Res.*, *91*(B2), 1961–1974.

Christensen, U. (1984), Convection with pressure-dependent and temperature-dependent non-Newtonian rheology, *Geophys. J. R. Astron. Soc.*, *77*(2), 343–384.

Christensen, U. (1995), Effects of phase-transitions on mantle convection, *Annu. Rev. Earth Planet. Sci.*, *23*, 65–87.

Cobden, L., S. Goes, M. Ravenna, E. Styles, F. Cammarano, K. Gallagher, and J. A. D. Connolly (2009), Thermochemical interpretation of 1-D seismic data for the lower mantle: The significance of nonadiabatic thermal gradients and compositional heterogeneity, *J. Geophys. Res.*, *114*, B11309, doi:10.1029/2008JB006262.

Conrad, C. P., B. Wu, E. I. Smith, T. A. Bianco, and A. Tibbetts (2010), Shear-driven upwelling induced by lateral viscosity variations and asthenospheric shear: A mechanism for intraplate volcanism, *Phys. Earth Planet. Inter.*, *178*(3-4), 162–175.

Cormier, M.-H., K. D. Gans, and D. S. Wilson (2011), Gravity lineaments of the Cocos Plate: Evidence for a thermal contraction crack origin, *Geochem. Geophys. Geosyst.*, *12*, Q07007, doi:10.1029/2011GC003573.

Doin, M. P., and L. Fleitout (1996), Thermal evolution of the oceanic lithosphere: An alternative view, *Earth Planet. Sci. Lett.*, *142*(1-2), 121–136.

Dumoulin, C., M. P. Doin, D. Arcay, and L. Fleitout (2005), Onset of small-scale instabilities at the base of the lithosphere: Scaling laws and role of pre-existing lithospheric structures, *Geophys. J. Int.*, *160*(1), 344–356.

Faccenna, C., T. W. Becker, S. Lallemand, Y. Lagabrielle, F. Funiciello, and C. Piromallo (2010), Subduction-triggered magmatic pulses: A new class of plumes?, *Earth Planet. Sci. Lett.*, *299*(1-2), 54–68.

Fukao, Y., and M. Obayashi (2013), Subducted slabs stagnant above, penetrating through, and trapped below the 660 km discontinuity, *J. Geophys. Res. Solid Earth*, *118*, 5920–5938, doi:10.1002/2013JB010466.

Gerya, T. V., and D. A. Yuen (2003), Rayleigh-Taylor instabilities from hydration and melting propel 'cold plumes' at subduction zones, *Earth Planet. Sci. Lett.*, *212*(1–2), 47–62.

Goes, S., F. A. Capitanio, G. Morra, M. Seton, and D. Giardini (2011), Signatures of downgoing plate-buoyancy driven subduction in Cenozoic plate motions, *Phys. Earth Planet. Inter.*, *184*(1-2), 1–13.

Gogus, O. H., and R. N. Pysklywec (2008), Near-surface diagnostics of dripping or delaminating lithosphere, *J. Geophys. Res.*, *113*, B11404, doi:10.1029/2007JB005123.

Gorczyk, W., T. V. Gerya, J. A. D. Connolly, and D. A. Yuen (2007), Growth and mixing dynamics of mantle wedge plumes, *Geology*, *35*(7), 587–590.

Griffiths, R. W. (1986), Dynamics of mantle thermals with constant buoyancy or anomalous internal heating, *Earth Planet. Sci. Lett.*, *78*, 435–446.

Hernlund, J. W., P. J. Tackley, and D. J. Stevenson (2008), Buoyant melting instabilities beneath extending lithosphere: 1. Numerical models, *J. Geophys. Res.*, *113*, B04405, doi:10.1029/2006JB004862.

Herzberg, C., P. D. Asimow, N. Arndt, Y. L. Niu, C. M. Lesher, J. G. Fitton, M. J. Cheadle, and A. D. Saunders (2007), Temperatures in ambient mantle and plumes: Constraints from basalts, picrites, and komatiites, *Geochem. Geophys. Geosyst.*, *8*, Q02006, doi:10.1029/2006GC001390.

Hieronymus, C. F., and D. Bercovici (1999), Discrete alternating hotspot islands formed by interaction of magma transport and lithospheric flexure, *Nature*, *397*(6720), 604–607.

Hieronymus, C. F., and D. Bercovici (2000), Non-hotspot formation of volcanic chains: control of tectonic and flexural stresses on magma transport, *Earth Plan. Sci. Lett.*, *181*(4), 539–554.

Hirose, K., F. Yingwei, M. Yanzhang, and M. Ho-Kwang (1999), The fate of subducted basaltic crust in the Earth's lower mantle, *Nature*, *397*(6714), 53–56.

Houseman, G. A., D. P. McKenzie, and P. Molnar (1981), Convective instability of a thickened boundary-layer and its relevance for the thermal evolution of Continental Convergent Belts, *J. Geophys. Res.*, *86*(NB7), 6115–6132.

Huang, J. S., S. J. Zhong, and J. van Hunen (2003), Controls on sublithospheric small-scale convection, *J. Geophys. Res.*, *108*(B8), 2405, doi:10.1029/2003JB002456.

Inoue, T., Y. Tanimoto, T. Irifune, T. Suzuki, H. Fukui, and O. Ohtaka (2004), Thermal expansion of wadsleyite, ringwoodite, hydrous wadsleyite and hydrous ringwoodite, *Phys. Earth Planet. Inter.*, *143*, 279–290.

Iwamori, H. (1991), Zonal structure of cenozoic basalts related to mantle upwelling in Southwest Japan, *J. Geophys. Res.*, *96*(B4), 6157–6170.

Jadamec, M. A., and M. I. Billen (2012), The role of rheology and slab shape on rapid mantle flow: Three-dimensional numerical models of the Alaska slab edge, *J. Geophys. Res.*, *117*, B02304, doi:10.1029/2011JB008563.

Johnson, R. W. (1989), *Intraplate Volcanism in Eastern Australia and New Zealand*, Cambridge Univ. Press. AQ4

Kameyama, M., and R. Nishioka (2012), Generation of ascending flows in the Big Mantle Wedge (BMW) beneath northeast Asia induced by retreat and stagnation of subducted slab, *Geophys. Res. Lett.*, *39*, L10309, doi:10.1029/2012GL051678.

Karato, S., and P. Wu (1993), Rheology of the upper mantle: A synthesis, *Science*, *260*(5109), 771–778.

Karato, S., M. R. Riedel, and D. A. Yuen (2001), Rheological structure and deformation of subducted slabs in the mantle transition zone: Implications for mantle circulation and deep earthquakes, *Phys. Earth Planet. Inter.*, *127*(1-4), 83–108.

Katsura, T., et al. (2004), Thermal expansion of Mg2SiO4 ringwoodite at high pressures, *J. Geophys. Res.*, *109*, B12209, doi:10.1029/2004JB003094.

King, S. D., and D. L. Anderson (1998), Edge-driven convection, *Earth Planet. Sci. Lett.*, *160*(3-4), 289–296.

King, S. D., and J. Ritsema (2000), African hot spot volcanism: Small-scale convection in the upper mantle beneath cratons, *Science*, *290*(5494), 1137–1140.

Korenaga, J., and T. H. Jordan (2004), Physics of multiscale convection in Earth's mantle: Evolution of sublithospheric convection, *J. Geophys. Res.*, *109*, B01405, doi:10.1029/2003JB002464.

Lei, J. (2012), Upper-mantle tomography and dynamics beneath the North China Craton, *J. Geophys. Res.*, *117*, B06313, doi:10.1029/2012JB009212.

Lei, J., D. Zhao, and Y. Su (2009), Insight into the origin of the Tengchong intraplate volcano and seismotectonics in southwest China from local and teleseismic data, *J. Geophys. Res.*, *114*, B05302, doi:10.1029/2008JB005881.

Lei, J., F. Xie, Q. Fan, and M. Santosh (2013), Seismic imaging of the deep structure under the Chinese volcanoes: An overview, *Phys. Earth Planet. Inter.*, *224*(0), 104–123.

Lei, J. S., and D. P. Zhao (2005), P-wave tomography and origin of the Changbai intraplate volcano in Northeast Asia, *Tectonophysics*, *397*(3-4), 281–295.

Liu, L., and D. R. Stegman (2012), Origin of Columbia River flood basalt controlled by propagating rupture of the Farallon slab, *Nature*, *482*(7385), 386–U1508.

Long, M. D., and P. G. Silver (2009), Mantle flow in subduction systems: The subslab flow field and implications for mantle dynamics, *J. Geophys. Res.*, *114*, B10312, doi:10.1029/2008JB006200.

Lustrino, M., and M. Wilson (2007), The circum-Mediterranean anorogenic Cenozoic igneous province, *Earth Sci. Rev.*, *81*(1-2), 1–65.

Moresi, L., S. Zhong, and M. Gurnis (1996), The accuracy of finite element solutions of Stokes' flow with strongly varying viscosity, *Phys. Earth Planet. Int.*, *97*(1-4), 83–94.

AGU Geochemistry, Geophysics, Geosystems 10.1002/2014GC005608

Morgan, W. J. (1972), Plate motions and deep mantle convection, *Geol. Soc. Am. Mem.*, *132*, 7–22.

Murakami, M., Y. Ohishi, N. Hirao, and K. Hirose (2012), A perovskitic lower mantle inferred from high-pressure, high-temperature sound velocity data, *Nature*, *485*(7396), 90–U118.

Piromallo, C., and C. Faccenna (2004), How deep can we find the traces of Alpine subduction?, *Geophys. Res. Lett.*, *31*, L06605, doi:10.1029/2003GL019288.

Piromallo, C., T. W. Becker, F. Funiciello, and C. Faccenna (2006), Three-dimensional instantaneous mantle flow induced by subduction, *Geophys. Res. Lett.*, *33*, L08304, doi:10.1029/2005GL025390.

Rabinowicz, M., S. Rouzo, J. C. Sempere, and C. Rosemberg (1993), 3-dimensional mantle flow beneath midocean ridges, *J. Geophys. Res.*, *98*(B5), 7851–7869.

Raddick, M. J., E. M. Parmentier, and D. S. Scheirer (2002), Buoyant decompression melting: A possible mechanism for intraplate volcanism, *J. Geophys. Res.*, *107*(B10), 2228, doi:10.1029/2001JB000617.

Richard, G. C., and D. Bercovici (2009), Water-induced convection in the Earth's mantle transition zone, *J. Geophys. Res.*, *114*, B01205, doi:10.1029/2008JB005734.

Richard, G. C., and H. Iwamori (2010), Stagnant slab, wet plumes and Cenozoic volcanism in East Asia, *Phys. Earth Planet. Inter.*, *183*(1-2), 280–287.

Richter, F. M., and B. Parsons (1975), On the interaction of two scales of convection in the mantle, *J. Geophys. Res.*, *80*(17), 2529–2541.

Riedel, M. R., and S. Karato (1997), Grain-size evolution in subducted oceanic lithosphere associated with the olivine-spinel transformation and its effects on rheology, *Earth Planet. Sci. Lett.*, *148*(1-2), 27–43.

Rubie, D. C. (1984), The olivine-spinel transformation and the rheology of subducting lithosphere, *Nature*, *308*(5959), 505–508.

Sakamaki, T., A. Suzuki, E. Ohtani, H. Terasaki, S. Urakawa, Y. Katayama, K.-i. Funakoshi, Y. Wang, J. W. Hernlund, and M. D. Ballmer (2013), Ponded melt at the boundary between the lithosphere and asthenosphere, *Nat. Geosci.*, *6*(12), 1041–1044.

Sakuyama, T., et al. (2013), Melting of dehydrated oceanic crust from the stagnant slab and of the hydrated mantle transition zone: Constraints from Cenozoic alkaline basalts in eastern China, *Chem. Geol.*, *359*, 32–48.

Sandwell, D. T., E. L. Winterer, J. Mammerickx, R. A. R. A. Duncan, M. A. Lynch, D. A. Levitt, and C. L. Johnson (1995), Evidence for diffuse extension of the Pacific plate from Pukapuka ridges and cross-grain gravity lineations, *J. Geophys. Res.*, *100*(B8), 15,087–15,100.

Shimojuku, A., T. Kubo, E. Ohtani, T. Nakamura, R. Okazaki, R. Dohmen, and S. Chakraborty (2009), Si and O diffusion in (Mg,Fe)2SiO4 wadsleyite and ringwoodite and its implications for the rheology of the mantle transition zone, *Earth Planet. Sci. Lett.*, *284*(1–2), 103–112.

Sigloch, K., N. McQuarrie, and G. Nolet (2008), Two-stage subduction history under North America inferred from multiple-frequency tomography, *Nat. Geosci.*, *1*(7), 458–462.

Strak, V., and W. P. Schellart (2014), Evolution of 3-D subduction-induced mantle flow around lateral slab edges in analogue models of free subduction analysed by stereoscopic particle image velocimetry technique, *Earth Planet. Sci. Lett.*, *403*, 368–379.

Tackley, P. J., and D. J. Stevenson (1993), A mechanism for spontaneous self-perpetuating volcanism on the terrestrial planets, in *Flow and Creep in the Solar System: Observations, Modeling and Theory*, edited by D. B. Stone and S. K. Runcorn, pp. 307–322, Kluwer Acad.

Tang, Y., M. Obayashi, F. Niu, S. P. Grand, Y. J. Chen, H. Kawakatsu, S. Tanaka, J. Ning, and J. F. Ni (2014), Changbaishan volcanism in northeast China linked to subduction-induced mantle upwelling, *Nat. Geosci.*, *7*(6), 470–475.

Torsvik, T. H., M. A. Smethurst, K. Burke, and B. Steinberger (2006), Large igneous provinces generated from the margins of the large low-velocity provinces in the deep mantle, *Geophys. J. Int.*, doi:10.1111/j.1365-246X.2006.03158.x. AQ5

Turcotte, D. L., and G. Schubert (1982), *Geodynamics: Applications of Continuum Physics to Geological Problems*, John Wiley, New York.

van der Meer, D. G., W. Spakman, D. J. J. van Hinsbergen, M. L. Amaru, and T. H. Torsvik (2010), Towards absolute plate motions constrained by lower-mantle slab remnants, *Nat. Geosci.*, *3*(1), 36–40.

Vaughan, P. J., and R. S. Coe (1981), Creep mechanism In Mg2GeO4: Effects of a phase-transition, *J. Geophys. Res.*, *86*(NB1), 389–404.

Wellman, P., and I. McDougall (1974), Cainozoic igneous activity in eastern Australia, *Tectonophysics*, *23*(1–2), 49–65.

Wilson, J. T. (1963), A possible origin of Hawaiian Islands, *Can. J. Phys.*, *41*(6), 863. AQ6

Wilson, M., and H. Downes (2006), Tertiary-Quaternary intra-plate magmatism in Europe and its relationship to mantle dynamics, in *European Lithosphere Dynamics*, edited by R. Stephenson and D. Gee, pp. 147–166, Geol. Soc. of London, London.

Xu, W., C. Lithgow-Bertelloni, L. Stixrude, and J. Ritsema (2008), The effect of bulk composition and temperature on mantle seismic structure, *Earth Planet. Sci. Lett.*, *275*(1-2), 70–79.

Yamazaki, D., T. Inoue, M. Okamoto, and T. Irifune (2005), Grain growth kinetics of ringwoodite and its implication for rheology of the subducting slab, *Earth Planet. Sci. Lett.*, *236*(3–4), 871–881.

Ye, Y., et al. (2012), Compressibility and thermal expansion of hydrous ringwoodite with 2.5(3) wt% H2O, *Am. Mineral.*, *97*(4), 573–582.

Yuan, K., and C. Beghein (2014), Three-dimensional variations in Love and Rayleigh wave azimuthal anisotropy for the upper 800 km of the mantle, *J. Geophys. Res. Solid Earth*, *119*, 3232–3255.

Zhao, D., Y. Tian, J. Lei, L. Liu, and S. Zheng (2009), Seismic image and origin of the Changbai intraplate volcano in East Asia: Role of big mantle wedge above the stagnant Pacific slab, *Phys. Earth Planet. Inter.*, *173*(3–4), 197–206.

Zhou, X., and R. L. Armstrong (1982), Cenozoic volcanic-rocks of Eastern China: Secular and geographic trends in chemistry and strontium isotopic composition, *Earth Planet. Sci. Lett.*, *58*(3), 301–329.

Zou, H., Q. Fan, and Y. Yao (2008), U-Th systematics of dispersed young volcanoes in NE China: Asthenosphere upwelling caused by piling up and upward thickening of stagnant Pacific slab, *Chem. Geol.*, *255*(1-2), 134–142.

AQ1 Please note that references "Richard and coworkers [2009; 2010]" and "Lei and Zhao [2005; 2009]" have been changed as "Richard and Bercovici [2009]; Richard and Iwamori [2010]" and "Lei and Zhao [2005]; Lei et al., [2009]," respectively as per details given in the list. Please check if this is OK.

AQ2 Please provide a descriptive title for Appendix A.

AQ3 Please note that equation given in appendix should be numbered separately and hence equation (3) has been changed as equation (A1) as per journal style. Please check.

AQ4 Please provide publisher location for references "Johnson [1989]" and "Tackley and Stevenson [1993]".

AQ5 Please provide volume number and page range for reference "Torsvik et al. [2006]".

AQ6 Please provide complete page range for reference "Wilson [1963]".

AQ7: Author: Please complete the Publication Fee Consent Form included with your article and return to the Production Editor with your proofs.

AQ8: Please confirm that given names (red) and surnames/family names (green) have been identified correctly.

WILEY-BLACKWELL

USING e-ANNOTATION TOOLS FOR ELECTRONIC PROOF CORRECTION

Required software to e-Annotate PDFs: Adobe Acrobat Professional or Adobe Reader (version 8.0 or above). (Note that this document uses screenshots from Adobe Reader X)
The latest version of Acrobat Reader can be downloaded for free at: http://get.adobe.com/reader/

Once you have Acrobat Reader open on your computer, click on the Comment tab at the right of the toolbar:

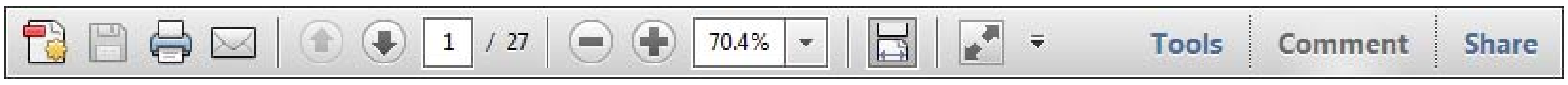

This will open up a panel down the right side of the document. The majority of tools you will use for annotating your proof will be in the Annotations section, pictured opposite. We've picked out some of these tools below:

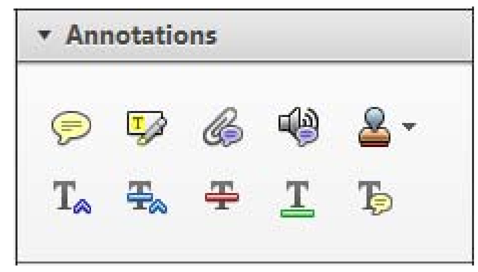

1. Replace (Ins) Tool – for replacing text.

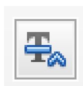

Strikes a line through text and opens up a text box where replacement text can be entered.

How to use it

- Highlight a word or sentence.
- Click on the Replace (Ins) icon in the Annotations section.
- Type the replacement text into the blue box that appears.

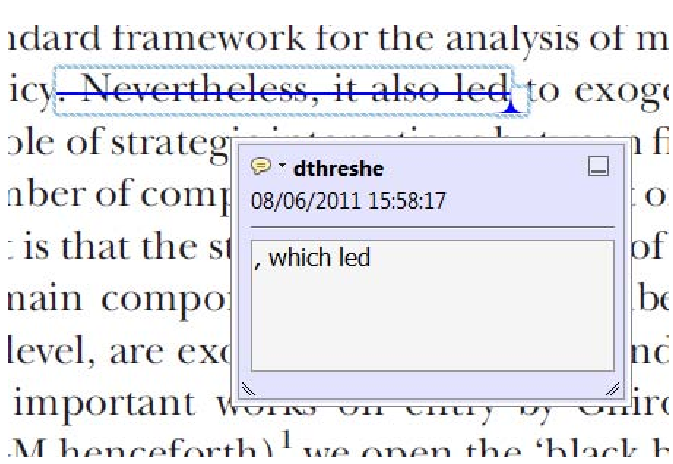

2. Strikethrough (Del) Tool – for deleting text.

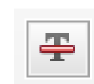

Strikes a red line through text that is to be deleted.

How to use it

- Highlight a word or sentence.
- Click on the Strikethrough (Del) icon in the Annotations section.

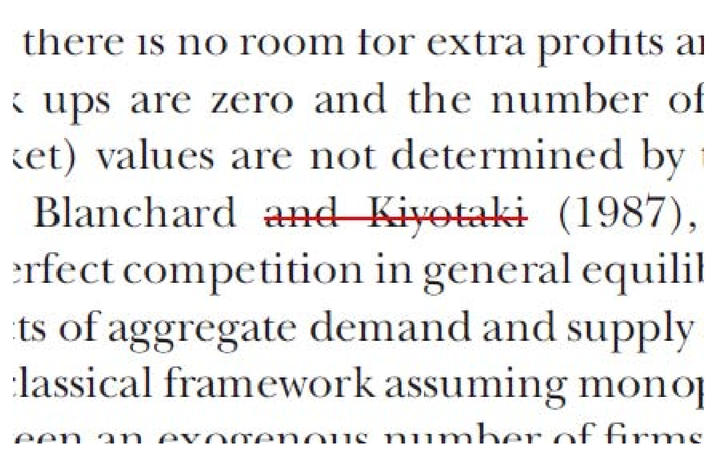

3. Add note to text Tool – for highlighting a section to be changed to bold or italic.

Highlights text in yellow and opens up a text box where comments can be entered.

How to use it

- Highlight the relevant section of text.
- Click on the Add note to text icon in the Annotations section.
- Type instruction on what should be changed regarding the text into the yellow box that appears.

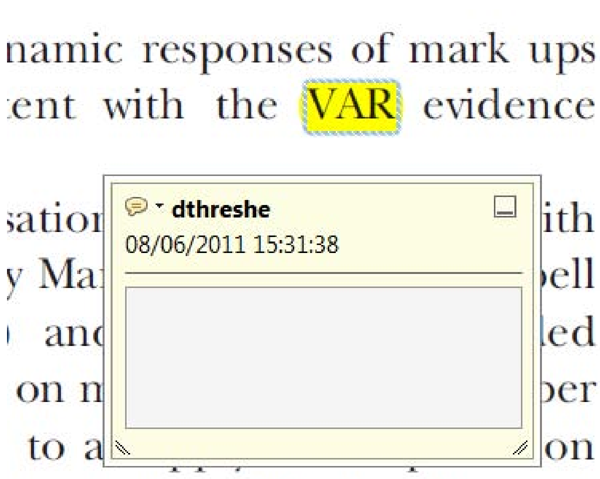

4. Add sticky note Tool – for making notes at specific points in the text.

Marks a point in the proof where a comment needs to be highlighted.

How to use it

- Click on the Add sticky note icon in the Annotations section.
- Click at the point in the proof where the comment should be inserted.
- Type the comment into the yellow box that appears.

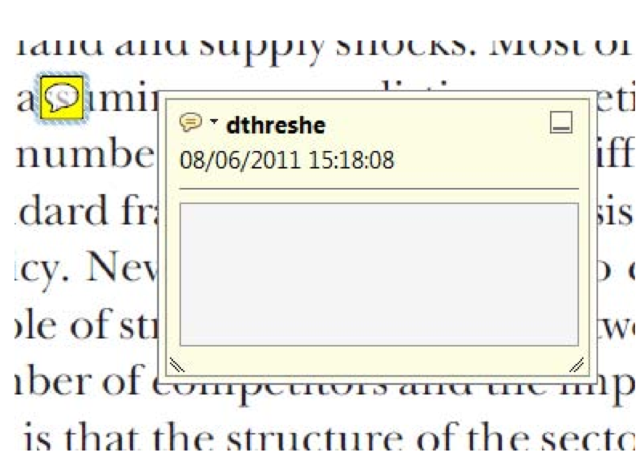

USING e-ANNOTATION TOOLS FOR ELECTRONIC PROOF CORRECTION

5. Attach File Tool – for inserting large amounts of text or replacement figures.

Inserts an icon linking to the attached file in the appropriate pace in the text.

How to use it

- Click on the Attach File icon in the Annotations section.
- Click on the proof to where you'd like the attached file to be linked.
- Select the file to be attached from your computer or network.
- Select the colour and type of icon that will appear in the proof. Click OK.

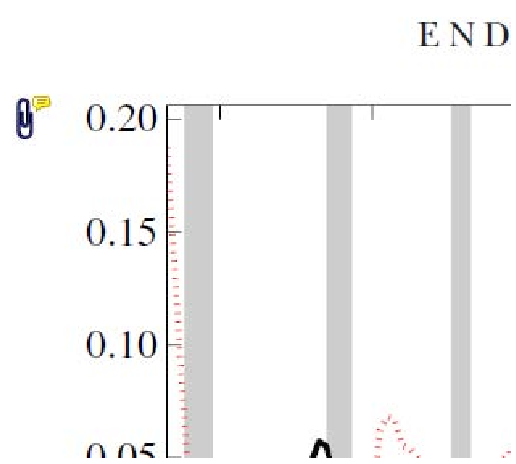

6. Add stamp Tool – for approving a proof if no corrections are required.

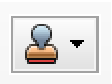

Inserts a selected stamp onto an appropriate place in the proof.

How to use it

- Click on the Add stamp icon in the Annotations section.
- Select the stamp you want to use. (The Approved stamp is usually available directly in the menu that appears).
- Click on the proof where you'd like the stamp to appear. (Where a proof is to be approved as it is, this would normally be on the first page).

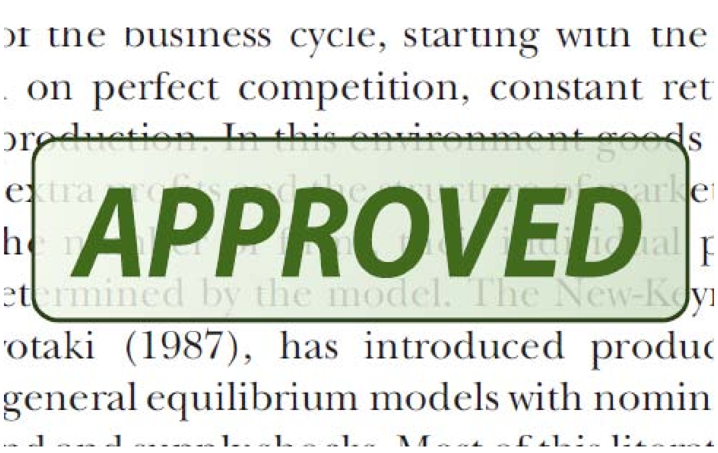

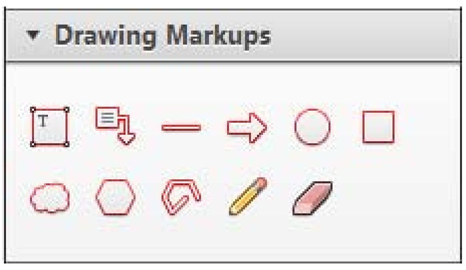

7. Drawing Markups Tools – for drawing shapes, lines and freeform annotations on proofs and commenting on these marks.

Allows shapes, lines and freeform annotations to be drawn on proofs and for comment to be made on these marks..

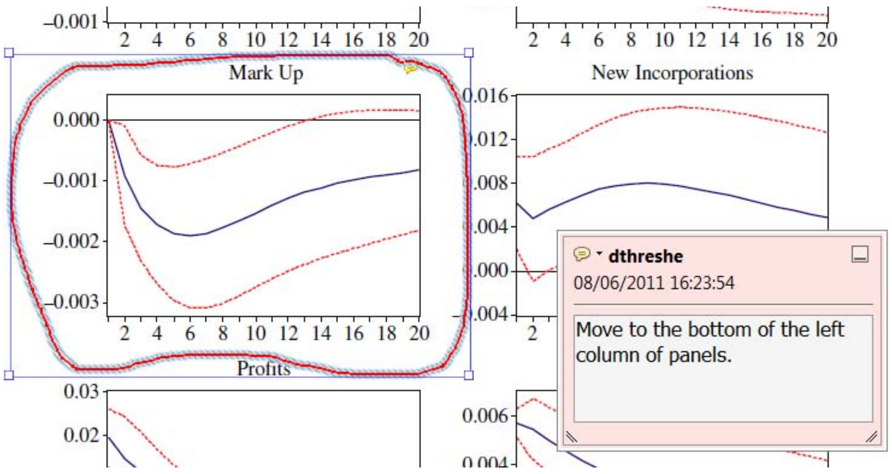

How to use it

- Click on one of the shapes in the Drawing Markups section.
- Click on the proof at the relevant point and draw the selected shape with the cursor.
- To add a comment to the drawn shape, move the cursor over the shape until an arrowhead appears.
- Double click on the shape and type any text in the red box that appears.

For further information on how to annotate proofs, click on the Help menu to reveal a list of further options: